THE EUROPEAN
PHYSICAL JOURNAL B

Check for
updates

Regular Article - Statistical and Nonlinear Physics

Power consumption during forward locomotion of C. elegans: an electrical circuit simulation

Sebastian Jenderny[1,a] , Karlheinz Ochs[1,b], and Philipp Hövel[2,c]

[1] Chair of Digital Communication Systems, Ruhr-Universität Bochum, Universitätsstraße 150, Bochum 44801, NRW, Germany
[2] Theoretical Physics and Center for Biophysics, Saarland University, Campus E2 6, Saarbrücken 66123, Saarland, Germany

© The Author(s) 2024

Abstract. Biological neuronal networks are of great interest for emerging technological approaches such as neuromorphic engineering due to their capability to efficiently process information. To understand the principles governing this energy efficiency, it is useful to investigate model organisms with small and well-characterized neuronal networks. *Caenorhabditis elegans* (*C. elegans*) is such a model organism and perfectly suited for this purpose, because its neuronal network consists of only 302 neurons whose interconnections are known. In this work, we design an ideal electrical circuit modeling this neuronal network in combination with the muscles it controls. We simulate this circuit by a run-time efficient wave digital algorithm. This allows us to investigate the energy consumption of the network occurring during locomotion of *C. elegans* and hence deduce potential design principles from an energy efficiency point of view. Simulation results verify that a locomotion is indeed generated. We conclude from the corresponding energy consumption rates that a small number of neurons in contrast to a high number of interconnections is favorable for consuming only little energy. This underlines the importance of interneurons. Moreover, we find that gap junctions are a more energy-efficient connection type than synapses, and inhibitory synapses consume more energy than excitatory ones. However, the energetically cheapest connection types are not the most frequent ones in *C. elegans*' neuronal network. Therefore, a potential design principle of the network could be a balance between low energy costs and a certain functionality.

1 Introduction

Due to its high computational power and efficient information processing, the human brain has attracted a lot of interest in the field of hardware-based artificial neural networks. However, great interest also lies in the study of much simpler neuronal networks, because unveiling core principles of neural information processing and fundamental, functional subcircuits is much easier in smaller networks. A popular choice for this purpose is the neuronal network of the nematode *Caenorhabditis elegans* (*C. elegans*), since it consists of only 302 neurons and its connectome is fully described. Of these 302 neurons, 282 neurons belong to the somatic system and 279 neurons are especially considered when studying its locomotion [1]. See appendix A for a list of the considered neurons and their type. This locomotion is associated with a sinusoidal-like wave motion of the worm. It is generated by 95 muscles, which are divided into dorsal left (DL), dorsal right (DR), ventral left (VL),

and ventral right (VR) muscles [2]. A sketch of *C. elegans* is shown in Fig. 1. Locomotion can be triggered by various touch sensors but is also linked to, e.g., the chemosensory system [3].

C. elegans as a model organism is not only relevant to biology, but also to technology and electrical circuits. For instance, it enables the derivation of locomotion-generating circuits for robotic applications [4]. Studying *C. elegans* and its neuronal network can also improve the control of robotics in the simultaneous presence of different stimuli, locomotion in *C. elegans* is generated while multiple types of sensory information are processed. Moreover, *C. elegans* also allows for studying the principles behind an information processing that is far more efficient than that of today's computers. Energy efficiency has for instance been studied with respect to the sparsity of a neuronal network [5,6]. Moreover, an energy homeostasis principle shaping the neuronal dynamics has been proposed in [7] by considering a balance between energy supply, energy costs, and availability of energy. Concerning *C. elegans*, energy-efficiency of a subset of its neuronal network coupled only via gap junctions has been investigated in [8].

[a] e-mail: sebastian.jenderny@ruhr-uni-bochum.de (corresponding author)
[b] e-mail: karlheinz.ochs@ruhr-uni-bochum.de
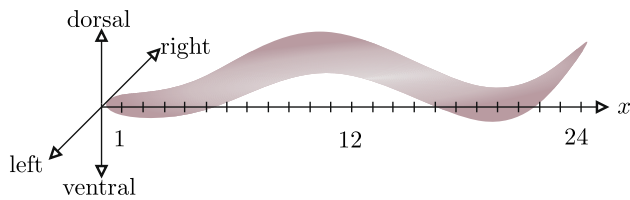[c] e-mail: philipp.hoevel@uni-saarland.de

Fig. 1 Illustration of the sinusoidal body shape during locomotion, with x denoting the muscle index per group (ventral left, ventral right, dorsal left, dorsal right)

Fig. 2 Differentiation of sensory neurons, motor neurons, and interneurons

In this work, our aim is to investigate the power consumption of the individual building blocks of *C. elegans*' neuronal network, i.e. synapses, gap junctions, and ion channels of neurons during locomotion behavior. To our utmost knowledge, such an analysis has not been considered for *C. elegans*. Based on this analysis, we can provide insights into a functional neuronal network topology design of *C. elegans* with respect to energy efficiency principles. This allows us to deduce potential design principles that can aid in designing more energy-efficient hardware-based neuronal networks. For this purpose, we model the neuronal network of *C. elegans* by an electrical circuit and derive a run-time efficient circuit simulation algorithm. Existing circuit realizations of C. elegans are for instance based on an FPGA emulation for leaky-integrate-and-fire models as neurons of *C. elegans* as part of the Si elegans project [9,10]. Moreover, a memristive circuit has recently been proposed for the locomotory neuronal network [4]. In contrast to these approaches, we design an ideal, bio-inspired electrical circuit based on analog circuit elements that accounts for the 279 somatic neurons and 95 body wall muscles. This offers several advantages. First, due to its analog nature, the circuit can potentially be used to extract electrical subcircuits that mimic functional, neuronal subnetworks of *C. elegans* for, e.g., specific motor control or sensory information processing tasks. Second, including the body wall muscles allows us to link the mimicked neuronal activity to locomotion behavior. Third, considering the 279 somatic neurons instead of only a subset, such as the locomotory circuit, enables us to take the influence of other neurons on the generation of locomotion into account. This way, we can derive network design principles for the entire somatic network with respect to a specific behavior, namely forward locomotion. To this end, we derive circuit models for neurons and for muscles and verify the resulting full system via wave digital simulations [11]. This framework has, for instance, been applied to simulate single neurons [12,13] and small neuronal networks [14], and provides a flexible, potentially real-time capable algorithm.

The rest of this paper is organized as follows: In Sects. 2 and 3, circuit models for the neurons and muscles are derived. Section 4 discusses the circuit realization of the interconnections between neurons as well as between neurons and muscles. Simulation results for the locomotion behavior as well as an analysis of the corre-

sponding energy consumption are presented in Sect. 5. Finally, conclusions are given in Sect. 6.

2 Neuron model

A detailed biology-based modeling of *C. elegans*' neuronal network is a very challenging task for two major reasons. First, as of now, electrophysiological recordings are not available for most neurons. Second, standard spiking neuron models have very limited applicability to the neurons of *C. elegans*. This is because the neurons of *C. elegans* were for long believed to not fire action potentials at all, but rather to be isopotential [15]. This is related to the fact that no sodium channels have been found in neurons of *C. elegans*, hinting that neuronal activity might be driven by voltage-gated calcium channels instead [15,16]. Up to now, action potentials have been found in the sensory neuron AWA [16,17] and in enteric motor neurons [18]. For these reasons, we use a generic modeling approach for the neurons by classifying them into three functional types: (i) sensory neurons that receive sensory signals via receptors, (ii) motor neurons that innervate and control muscles, and (iii) interneurons that relay signals between sensory and motor neurons, see Fig. 2.

Here, neurons of the same type show the same behavior. The classification is based on [19], where a list of all neurons and their types can be found. Note that some neurons play multiple roles, e.g., there can be sensory-motor neurons. Since we consider a strict classification, we treat potential sensory inter and inter motor neurons as purely interneurons. Moreover, we consider all sensory neurons that are also motor neurons to be purely motor neurons. In total, this leads to 104 motor neurons, 96 interneurons, and 79 sensory neurons, cf. A.

Let us now define the activity patterns of the three classes as follows: (i) Interneurons most likely show isopotential behavior [15,20,21], which we assume for all interneurons in our modeling approach. (ii) Motor neurons related to the locomotion show oscillatory behavior [22], but no action potentials have been found [18]. However, at least in the neuron RMD, plateau potentials have been found [15,20]. We assume this behavior for all motor neurons. (iii) Action potentials have been found for the sensory neuron AWA, which is why we model all sensory neurons to generate action potentials. As a generic neuron model, we make use of the Morris–Lecar model, since it offers several advantages. First, it is a biologically reasonable model that is computationally simpler than, e.g., Hodgkin-Huxley models. Second, it naturally comes with a calcium instead of a sodium channel, which is more precise
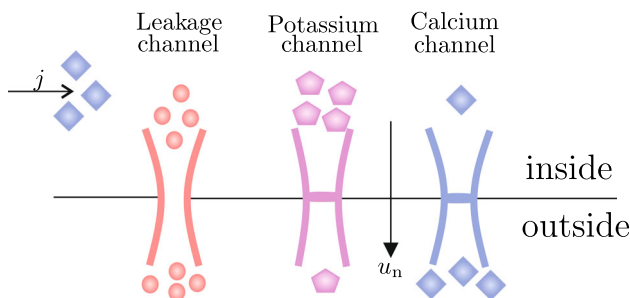
Fig. 3 Electrochemical processes taking place at a cell membrane, e.g., of neurons, which is currently in its resting state. j and u_n denote the input current and membrane potential, respectively

Fig. 4 Morris–Lear circuit corresponding to Eqs. (1)

when accounting for *C. elegans* neurons. Third, the Morris–Lecar modeling framework is a conductance-based model and is thus directly interpretable as an electrical circuit. The circuit representation also allows us to directly calculate power flows, which we require for the investigation of energy consumption. The Morris–Lecar model is based on the electrochemical processes observed from an electrically excitable cell membrane visualized in Fig. 3.

Non-voltage-dependent ion transport mechanisms are summarized as leakage channels, while calcium and potassium channels only let their specific ions pass through if the membrane potential measured between the inside and the outside is large enough. These voltage levels are met when ions due to an input current enter the region of the channels. This current can stem from various sources such as synaptic transmission, electrical coupling via channels called gap junctions, or in the case of sensory neurons from sensory receptors. This behavior is mathematically described by the following set of differential equations [23,24]:

$$C_\mathrm{n}\dot{u}_\mathrm{n} = j_\mathrm{n} + j_\mathrm{t} - i_\mathrm{K} - i_\mathrm{Ca} - i_\mathrm{L} \tag{1a}$$

$$i_\mathrm{Ca} = g_\mathrm{Ca}(u_\mathrm{n})\left[u_\mathrm{n} - E_\mathrm{Ca}\right] \tag{1b}$$

$$i_\mathrm{K} = W_\mathrm{K}\left[u_\mathrm{n} - E_\mathrm{K}\right], \quad W_\mathrm{K}(z) = zG_\mathrm{K} \tag{1c}$$

$$i_\mathrm{L} = G_\mathrm{L}\left[u_\mathrm{n} - E_\mathrm{L}\right] \tag{1d}$$

$$g_\mathrm{Ca}(u_\mathrm{n}) = \frac{G_\mathrm{Ca}}{2}\left[1 + \tanh\left(\frac{u_\mathrm{n} - U_\mathrm{Ca,1}}{U_\mathrm{Ca,2}}\right)\right] \tag{1e}$$

$$\dot{z} = \left[z_\infty(u_\mathrm{n}) - z\right] F \cosh\left(\frac{u_\mathrm{n} - U_\mathrm{K,1}}{2U_\mathrm{K,2}}\right) \tag{1f}$$

$$z_\infty(u_\mathrm{n}) = \frac{1}{2}\left[1 + \tanh\left(\frac{u_\mathrm{n} - U_\mathrm{K,1}}{U_\mathrm{K,2}}\right)\right]. \tag{1g}$$

Here, the membrane potential u_n and the fraction of open potassium channels z are the dynamical variables. C_n is the membrane capacitance, j_n is the input current due to synapses and gap junctions, and j_t is the input current due to a sensed touch. Furthermore, i_K, i_Ca, and i_L denote the potassium current, calcium current, and leakage current, respectively. G_L and E_L are the conductance of the leakage channel and its resting potential, respectively. $g_\mathrm{Ca}(u_\mathrm{n}), G_\mathrm{Ca}, U_\mathrm{Ca,1}$, and $U_\mathrm{Ca,2}$
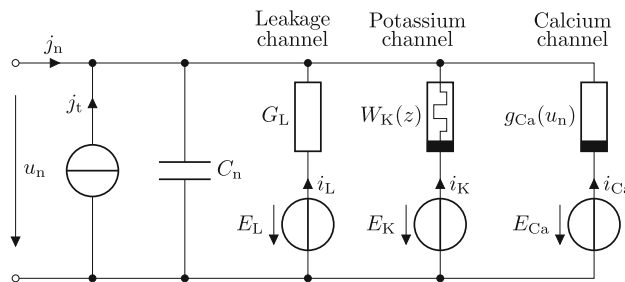
are the conductance of the calcium channel, its maximum conductance, the threshold voltage, and the edge steepness for the opening of the channel, respectively. W_K denotes the memductance of the potassium channel, cf. [24], G_K is its maximum conductance and z_∞ describes the fraction of open channels when the membrane potential is equal to its resting potential. F is the opening rate of the potassium channel, $U_\mathrm{K,1}$ is the corresponding threshold voltage, and $U_\mathrm{K,2}$ refers to the corresponding edge steepness. Note that the potassium channel has originally been considered as a nonlinear conductance, but has later been identified to be a memristor [24]. We adopt this understanding for this work. The corresponding circuit is shown in Fig. 4.

In the following, we briefly discuss the specific modeling of sensory, inter, and motor neurons. As the action potentials observed for the neuron AWA are in the order of milliseconds [16], we use a scaled version of the parameters presented in [12] for the sensory neurons. For the interneurons, we strongly decrease the maximum conductance value G_K such that no action potentials arise. Considering the motor neurons, we design the parameters such that action potentials with long-lasting phases of positive membrane potential are present. The duration of these action potentials is congruent with those of enteric motor neurons, which have been reported to be in the order of seconds [18]. The parameters used throughout this paper are listed in Table 1. They are roughly in the same order of magnitude as parameters for biophysically detailed modeling of specific neurons of *C. elegans* [25].

Exemplary membrane potential behavior for all three types is shown in Fig. 5, where each neuron is stimulated by a current pulse lasting for 1.7 s. As can be seen, sensory neurons generate short action potentials with a high frequency, while motor neurons generate an action potential that lasts approximately 1s. Lastly, the membrane potential of interneurons rapidly increases to a positive voltage, but they do not generate spikes and remain at this voltage until the current stimulus is turned off. This behavior is approximately comparable to that of an RC circuit.

So far, the circuit model for the neurons only allows for observing membrane potentials and ion currents. Membrane potentials are typically considered as the output signal of neurons, but cannot always be measured because electrophysiological recordings can be difficult to conduct. Instead, fluorescence traces of neu-
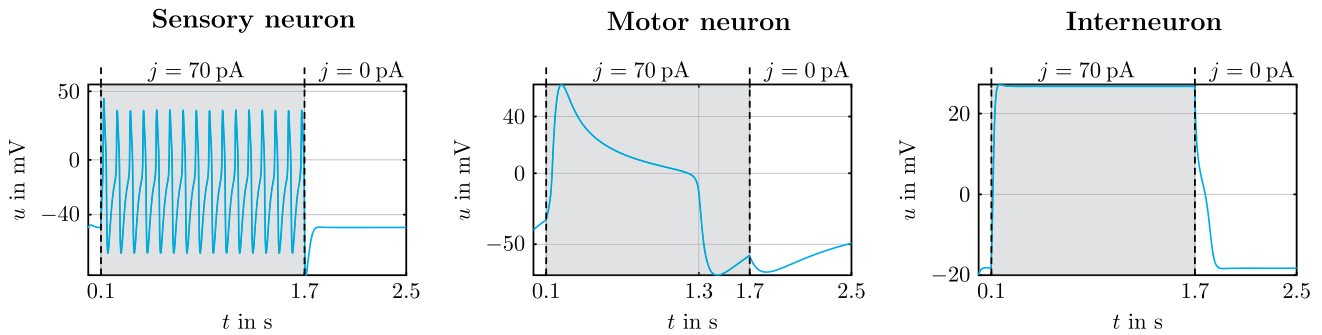
Fig. 5 Membrane potentials of sensory, inter, and motor neurons. The gray shaded areas highlight the time for which a constant current stimulus j is applied

Table 1 Neuron and muscle circuit parameters

Sensory neurons							
G_L	= 1	nS	G_{Ca} = 4.6 nS	G_K	= 7	nS
E_L	= −43	mV	ECa = 111 mV	E_K	= −119	mV
C	= 22	pF	$U_{Ca,1}$ = −1 mV	$U_{K,1}$	= 0	mV
			$U_{Ca,2}$ = 12 mV	$U_{K,2}$	= 23	mV
				F_K	= 30	Hz
Interneurons						
G_L	= 3	nS	G_{Ca} = 1 nS	G_K	= 0.1	nS
E_L	= −20	mV	ECa = 111 mV	E_K	= −119	mV
C	= 22	pF	$U_{Ca,1}$ = −1 mV	$U_{K,1}$	= 0	mV
			$U_{Ca,2}$ = 12 mV	$U_{K,2}$	= 23	mV
				F_K	= 30	Hz
Motor neurons						
G_L	= 1.5	nS	G_{Ca} = 4.6 nS	G_K	= 7	nS
E_L	= −30	mV	ECa = 111 mV	E_K	= −119	mV
C	= 220	pF	$U_{Ca,1}$ = −9 mV	$U_{K,1}$	= 0	mV
			$U_{Ca,2}$ = 12 mV	$U_{K,2}$	= 23	mV
				F_K	= 1	Hz
Muscle circuit						
C_m	= 100	pS	G_0 = 1 nS	I_m	= 1	pA

rons are recorded via calcium imaging. To take this second type of output signal into account, we extend our circuit to model fluorescence traces as well. Note that for the artificially generated fluorescence traces to be comparable to real measurements, stimuli perceived by the recorded worm have to be known. This is not the case for existing recordings of freely moving animals reported in, e.g., [26–28]. For this reason, we focus on forward locomotion induced by a gentle touch, for which the sensory input is known to be primarily perceived by the neurons PLML and PLMR (cf. A).

We model the generation of fluorescence values based on calculating the calcium concentration changes occurring due to the neuronal activity. The dynamics of the calcium concentration η_{Ca} can be described by

$$\dot{\eta}_{Ca} = \alpha \left[i_{Ca} - i_{Ca,rest} \right] - \frac{1}{\tau} \left[\eta_{Ca} - \eta_{Ca,rest} \right] , \quad (2)$$

see [13], with the resting concentration η_{rest}, the calcium current i_{Ca} as well as its resting value $i_{Ca,rest}$, and the decay time τ. Moreover, α is a factor for converting
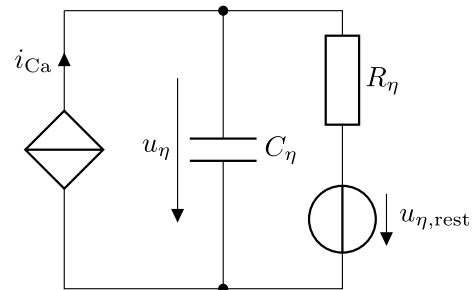

Fig. 6 RC circuit for calculating the calcium concentration

current into concentration change, which we choose to be $\alpha = 10^3 \frac{\text{mol}}{\text{m}^3\text{C}}$.

Following [13], Eq. (2) can be realized by an equivalent RC circuit governed by

$$\dot{u}_\eta = \frac{1}{C_\eta} i_{Ca} - \frac{1}{R_\eta C_\eta} \left[u_\eta - U_{\eta,rest} \right] , \quad (3a)$$

$$U_{\eta,rest} = k \left[\tau \alpha i_{Ca,rest} + \eta_{Ca,rest} \right] , \quad (3b)$$

$$C_\eta = \frac{1}{k\alpha} , \quad R_\eta = k\tau\alpha , \quad k = 1 \frac{\text{Vm}^3}{\text{mol}} . \quad (3c)$$

Here, u_η is a voltage representing the calcium concentration, $U_{\eta,rest}$ is a constant voltage, C_η is a capacitance, R_η is a resistance, and k is a normalization constant.

Note that since the Morris–Lecar circuit already provides calcium current, we can directly extend this circuit with the RC circuit by interconnecting them via a current follower. The RC circuit is shown in Fig. 6, where the current follower is represented as a controlled current source.

Given the calcium concentrations, we can now calculate fluorescence values. In general, calcium concentration can be inferred from fluorescence via

$$\Delta\eta_{Ca} = K_D \frac{F_{max}}{F_0} \frac{\left[1 - D_F^{-1} \right] \Delta F / F_0}{\left[\frac{\Delta F_{max}}{F_0} - \frac{\Delta F}{F_0} \right] \frac{\Delta F_{max}}{F_0}} , \quad (4a)$$

$$\Delta\eta_{Ca} = \eta_{Ca} - \eta_{Ca,rest} , \quad \Delta F = F - F_0 , \quad (4b)$$

$$\frac{\Delta F_{\max}}{F_0} = \frac{1 - D_F^{-1}}{D_F^{-1} + \bar{\eta}_{\mathrm{Ca}}/K_{\mathrm{D}}} \,, \tag{4c}$$

$$\Delta F_{\max} = F_{\max} - F_0 \,, \tag{4d}$$

see [29,30]. F is the fluorescence, K_{D} is the dissociation constant, D_{F} is the dynamic range of the fluorescence, $F_{\max}$ is the maximum fluorescence value, and F_0 is the baseline value of the fluorescence. ΔF and $\Delta F_{\max}$ are the fluorescence and maximum fluorescence without the baseline value, and $\Delta F/F_0$ is the normalized fluorescence change. By solving for $\Delta F/F_0$, we obtain

$$\Delta F/F_0 = \frac{\Delta \eta_{\mathrm{Ca}} \left[1 - D_F^{-1}\right]}{\eta_{\mathrm{Ca}} \left[D_F^{-1} + \eta_{\mathrm{Ca,rest}}/K_{\mathrm{D}}\right]} \,, \tag{5}$$

which can be seen as a post-processing of the calcium concentration provided by the RC circuit. Note that for this work, we assume the usage of the calcium indicator GCaMP6s, which is a popular choice for calcium imaging. Due to this, we choose $D_F = 63.2$, $K_{\mathrm{D}} = 144\,\mathrm{nM}$, and $\tau = 0.79\,\mathrm{s}$ based on [31]. Moreover, we assume a resting calcium concentration of $\eta_{\mathrm{Ca,rest}} = 50\,\mathrm{nM}$ which is a typical value for the neurons [25].

3 Muscle model

In this section, we derive an electrical circuit for the muscular behavior of *C. elegans*' locomotion. Existing modeling approaches for the muscular behavior focus on the muscle activation as well as on the mechanical interconnection of the muscles, see [32–34]. Since this work investigates the energy consumption of the neuronal information processing during forward locomotion, the muscle model mainly serves to verify that locomotion is generated. As such, a detailed biomechanical model is not required. Instead, we focus on a simple muscle activity model. Here, we take the muscle activity as a direct representation of the behavior. Based on [1,32], the muscle activity can be described by the leaky integrator

$$\dot{m} = \frac{1}{\tau_m} \left[1 - m + f(u_{\mathrm{n}})\right] \,, \tag{6}$$

where m is the dimensionless muscle activity that physically captures the muscular calcium concentration [35]. $\tau_m = 100\,\mathrm{ms}$ accounts for the muscle response time [1], and $f(u_{\mathrm{n}})$ is a function that accounts for synaptic inputs. Since this is a first-order differential equation, the muscle activity can be modeled by an equivalent RC circuit governed by

$$C_m \dot{u}_m = I_m + j_m(u_{\mathrm{n}}) - G_0 u_m \,, \tag{7}$$

$$C_m = \tau_m G_0 \,, \quad I_m = I_0 \,, \tag{8}$$

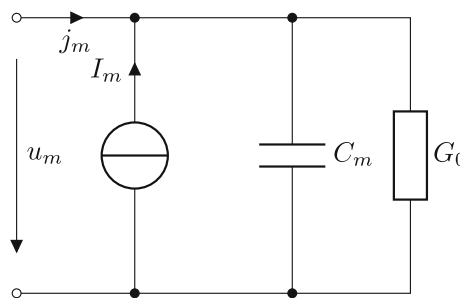with the capacitance C_m, the voltage u_m representing the muscle activity, a constant current I_m, the input

Fig. 7 RC-Circuit modeling the activity of a single muscle

currents due to synapses $j_m(u_{\mathrm{n}})$, a normalization conductance G_0 and a normalization current I_0. The resulting muscle circuit hence consists of an ideal current source, a capacitance, and a conductance, and is illustrated in Fig. 7.

4 Interconnection network

In this section, we discuss the interconnection network of neuron and muscle circuits to model the generation of forward locomotion. While a distinct locomotory circuit is known, we use the full connectome for the interconnection network. The latter can be described via adjacency matrices, which we have taken from [1]. Making use of the full connectome allows us to not only investigate the energy consumption of the locomotory circuit but also to compare it to the energy consumption of the complete network. The locomotory circuit primarily responsible for the forward locomotion of *C. elegans* is depicted in Fig. 8.

It consists of the sensory neurons PLM responsible for sensing a gentle touch, interneurons PVC and AVB, as well as motor neurons. The latter are divided into the first layer motor neurons VB and DB, acting excitatory on the muscles, and the second layer motor neurons VD and DD, inhibiting muscle activity. Note that some neurons are associated with the ventral or dorsal side of the worm, which is indicated by the letters V and D, respectively.

In this work, we model connections between neurons as either gap junctions or synapses, and interconnections between neurons and muscles only as synapses. We neglect muscle-to-muscle interconnections, as this coupling is typically considered to be weak in comparison to the synaptic ones [1]. In the following, let us first consider the neuronal interconnections. In the electrical circuit of the μ-th neuron described by equations (1) and (4), these interconnections are accounted for via the current $j_{\mathrm{n},\mu}$

$$j_{\mathrm{n},\mu} = j_{\mathrm{g},\mu} + j_{\mathrm{s},\mu} \,, \quad \mu = 1, \ldots, N \tag{9a}$$

$$j_{\mathrm{g},\mu} = G_{\mathrm{el}} \sum_{k=1}^{N} \left[u_{\mathrm{n},k} - u_{\mathrm{n},\mu}\right] a_{\mu k}^{\mathrm{el}} \,, \tag{9b}$$
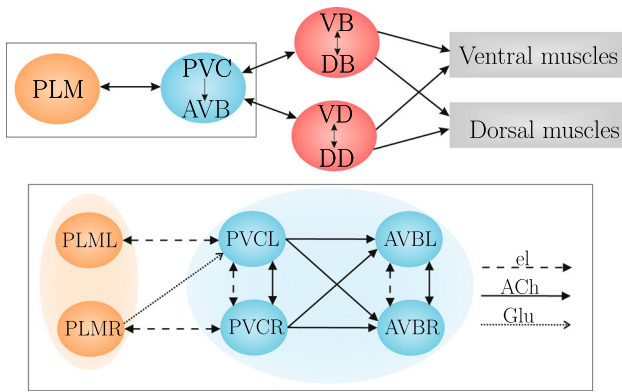
Fig. 8 Neuronal subcircuit for forward locomotion, with sensory neurons, interneurons, and motor neurons in orange, blue, and red, respectively. Neuron names are composed of abbreviations for the anatomical positions and the subgroup of neurons, i.e., posterior lateral microtubule (PLM), posterior ventral process C (PVC), anterior ventral process B (AVB), dorsal B-type motor neuron (DB), dorsal D-type motor neuron (DD), ventral B-type motor neuron (VB), and ventral D-type motor neuron (VD) [19]. An excerpt of the corresponding interconnection network is depicted at the bottom, with additional letters for the neuron names indicating whether neurons are located on the left or right side of the worm's body. The complete interconnection network is shown in [1]
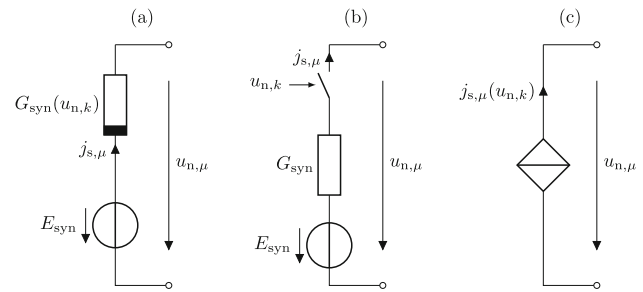

Fig. 9 Circuit models for neuronal synapses. **a** Equivalent circuit of neuronal synapses typically found in literature. **b** Equivalent circuit of neuronal synapses realized with a voltage-controlled switch. **c** Circuit representation of neuronal synapses as arbitrary voltage-controlled current sources

$$S(u_{n,k}) = \left[1 + e^{-[u_{n,k}-U_{s1}]/U_{s2}}\right]^{-1}. \quad (10e)$$

Here, G_{Glu}, G_{ACh}, and G_{GABA} are the coupling strengths for the neurotransmitters Glu, ACh, and GABA, respectively, E_{exc} denotes the resting potential for an excitatory synapse, and E_{inh} is the resting potential for an inhibitory synapse. $a_{n,\mu k}^{Glu}, a_{n,\mu k}^{ACh}$, and $a_{n,\mu k}^{GABA}$ are the μk-th elements of the adjacency matrices $\mathbf{A}_n^{Glu}, \mathbf{A}_n^{ACh}$, and $\mathbf{A}_n^{GABA}$, respectively, which describe the connections between neurons due to the corresponding type of neurotransmitter. Finally, $S(u_n)$ is the synaptic activation function, with the threshold voltage U_{s1} and a voltage determining the slope U_{s2}.

Individual synapses are typically represented by nonlinear resistive voltage sources, see Fig. 9a. Here, the nonlinear resistor can be realized by a voltage-controlled switch in series to a constant resistor G_{syn}, where the switch accounts for the synaptic activation function and can be realized by, e.g., transistors, cf. [36] for a comparable transistor-based approach. This is illustrated in Fig. 9b. G_{syn} depends on the type of neurotransmitter and is a multiple of either G_{Glu}, G_{ACh}, or G_{GABA}. The exact factor depends on the weight of the specific adjacency matrix entry. For our circuit simulation, we treat the synapses as voltage-controlled current sources shown in Fig. 9c, allowing for a generic circuit simulation.

where N is the total amount of neurons. $j_{g,\mu}$ is the input current caused by gap junctions, $j_{s,\mu}$ is the synaptic current, G_{el} is the associated coupling strength, and $a_{\mu k}^{el}$ is the μk-th element of the weighted adjacency matrix $\mathbf{A}_{el}$ that describes the gap-junction-based connections from neuron k to neuron μ. In our electrical circuit, for each positive entry in the adjacency matrix $\mathbf{A}_{el}$, we interconnect the corresponding neuron circuits with a constant series resistor. Note that the absolute resistance values differ for the individual gap junctions because there can be multiple gap junctions between a pair of neurons. This is reflected in the weight of the adjacency matrix.

The synaptic current $j_{s,\mu}$ is composed of the Glu current $j_{n,\mu}^{Glu}$, the ACh current $j_{n,\mu}^{Glu}$, and the GABA current $j_{n,\mu}^{Glu}$, which yields

$$j_{s,\mu} = j_{n,\mu}^{Glu} + j_{n,\mu}^{ACh} + j_{n,\mu}^{GABA} \quad (10a)$$

$$j_{n,\mu}^{Glu} = \sum_{k=1}^{N} S(u_{n,k})G_{Glu}\, a_{n,\mu k}^{Glu}\,[u_{n,\mu} - E_{exc}], \quad (10b)$$

$$j_{n,\mu}^{ACh} = \sum_{k=1}^{N} S(u_{n,k})G_{ACh}\, a_{n,\mu k}^{ACh}\,[u_{n,\mu} - E_{exc}], \quad (10c)$$

$$j_{n,\mu}^{GABA} = \sum_{k=1}^{N} S(u_{n,k})G_{GABA}\, a_{n,\mu k}^{GABA}\,[u_{n,\mu} - E_{inh}], \quad (10d)$$

Similar to the synapses between neurons, we model the neuromuscular synaptic currents via

$$j_{m,\mu} = \sum_{k=1}^{M} u_{n,k}\left[G_{ACh}\, a_{m,\mu k}^{ACh} + G_{GABA}\, a_{m,\mu k}^{GABA}\right], \quad (11)$$

where $j_{m,\mu}$ is the synaptic input current of the μ-th muscle, with $\mu = 1,\ldots,M$ and the total number of muscle cells M. $a_{m,\mu k}^{ACh}$ and $a_{m,\mu k}^{GABA}$ are the μk-th elements of the adjacency matrices $\mathbf{A}_m^{ACh}$ and $\mathbf{A}_m^{GABA}$, respectively, which denote the synaptic couplings from neurons to muscles based on ACh and GABA transmitters, respectively.
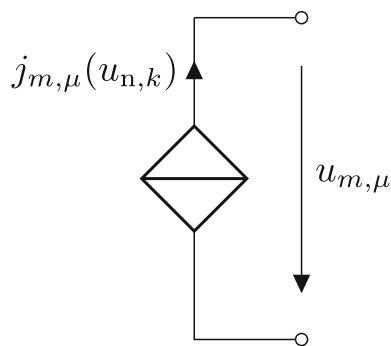
Fig. 10 Voltage-controlled current source as a circuit model for synapses between neurons and muscles

Fig. 11 Complete circuit model for mimicking the locomotory behavior of *C. elegans*. Note that the individual circuits are vector-valued variants of the Morris–Lecar circuit in Fig. 4, the calcium concentration circuit in Fig. 6, the muscle circuit in Fig. 7, the neuronal synapses in Fig. 9c, and the neuromuscular synapses in Fig. 10

Since the muscle model is not biologically accurate, it does not include synaptic ion channels as it is the case for the neuronal synapses. Instead, the muscular synaptic current is directly calculated as the product of the neuronal membrane potential u_n and the coupling strength of the synapse-specific neurotransmitter. From a circuit-theoretical point of view, this results in a voltage-to-current converter and can be represented by a voltage-controlled current source as well, see Fig. 10.

5 Simulating locomotion and analysis of power consumption

Let us now discuss the simulation of the combined circuit model. Taking all interconnections into account leads to a highly complex circuit diagram that requires great effort to simulate it via circuit simulation techniques like SPICE. To reduce this complexity, we consider vector-valued neuron and muscle models by virtually stacking, e.g., N Morris–Lecar circuits on top of each other to model N neurons. This approach results in the complete circuit model illustrated in Fig. 11 and is composed of vector-valued subcircuits for neurons, calcium concentration calculation, muscles, and interconnection elements introduced in the previous sections. The vector-valued nature of the complete circuit is advantageous for our simulation approach based on the wave digital concept [11]. In particular, a vector-valued representation makes the complete circuit model generic, as in this case more neurons and muscles only scale the dimensions of the corresponding subcircuits. As such, it enables an improved run-time efficiency of the simulation approach. Details about the wave digital concept are provided in the following.

5.1 Wave digital algorithm

We obtain simulation results using a wave digital algorithm implemented in MATLAB. Compared to other simulation techniques such as SPICE or ODE solvers, this provides us with a run-time efficient, real-time capable algorithm that has a direct correspondence
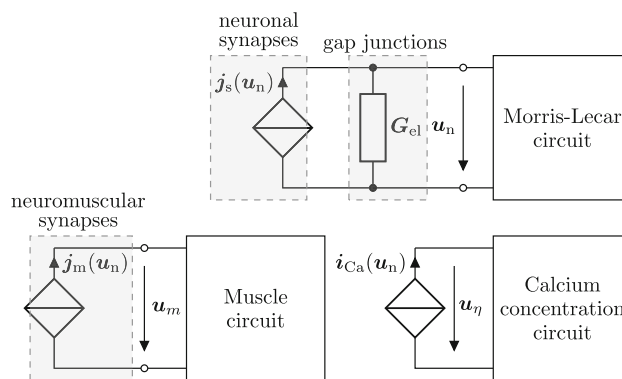
with the reference circuit. In particular, the algorithm can be derived from the equivalent electrical circuit by first decomposing the circuit into its ports and then translating the ports as well as the interconnection structure using the bijective transformation

$$a = u + Ri\,, \quad b = u - Ri\,, \quad R > 0\,, \tag{12}$$

see [11]. Here, a, b, and R are the incident wave, the reflected wave, and the port resistance, respectively. To translate the complete circuit of Fig. 11, we consider the subcircuits individually and start with the Morris–Lecar circuit. A corresponding scalar wave digital has been derived in [12,13] and its extension to vector-valued models is achieved when applying the bijective transformation to vectors of voltages and currents instead of scalar ones. This has for instance been used in [14] to couple Morris–Lecar circuit networks of arbitrary size. It is based on a general adaptor that represents arbitrary Kirchhoff interconnections, see [37,38]. This adaptor takes the incidence matrix of the interconnection structure as topology information and connects the Morris–Lecar circuits with the chosen coupling element. This is directly applicable to the interconnection network via gap junctions presented in this work, with the vector-valued resistor $\boldsymbol{G}_\mathrm{el} = G_\mathrm{el}\boldsymbol{A}_\mathrm{el}$ as coupling element. To connect this resistor to the vector-valued Morris–Lecar circuit, the adjacency matrix $\boldsymbol{A}_\mathrm{el}$ is translated into a corresponding incidence matrix that is used for the general adaptor. The wave digital equivalent of the resistor then corresponds to

$$\boldsymbol{b} = \boldsymbol{0}\,, \tag{13}$$

given that its port resistance matrix is chosen to $\boldsymbol{R} = \boldsymbol{1}/G_\mathrm{el}$, where $\boldsymbol{1}$ is the unity matrix. The interconnection network for the neuronal synapses consists of the vector-valued controlled current source $\boldsymbol{j}_\mathrm{s}(\boldsymbol{u}_\mathrm{n})$ that is translated by applying the bijective transformation. Its

wave digital equivalent is

$$\boldsymbol{a} = \boldsymbol{b} + 2\boldsymbol{R}\boldsymbol{j}_{\mathrm{s}}(\boldsymbol{u}_{\mathrm{n}}) \tag{14}$$

and is interconnected to the Morris–Lecar circuit via a parallel adaptor - the wave digital equivalent of a parallel connection, see [11] for more details.

A wave digital model of a scalar calcium concentration circuit has been presented in [13] and can also be extended to a vector-valued variant by considering vectors of voltages and currents for the wave digital translation. The translation of the muscle circuit works similarly, since both the muscle circuit and the calcium concentration circuit are essentially RC circuits. The muscle circuits' interconnection structure is given by the controlled current source $\boldsymbol{j}_m(\boldsymbol{u}_{\mathrm{n}})$ whose translation is identical to equation (14). This current source is again connected to the muscle circuit via a parallel adaptor.

To implement the wave digital equivalents of the individual subcircuits as a wave digital algorithm, the nonlinearities contained in the subcircuits have to be specially considered. This is because these nonlinearities give rise to implicit relationships between the incident and reflected wave of a port, known as delay-free loops. It is in general advisable to prevent as many loops as possible from arising, since typical solution approaches via iterative approaches [39–41] pose an increased computational effort. Delay-free loops can be prevented via reflection-free ports of the parallel adaptors [11], but also via source transformation of the nonlinearities contained in the Morris–Lecar model, see [12]. We deploy fixed-point iterations based on [39] for the remaining delay-free loops.

5.2 Neuronal and muscular activity

As an input signal, we apply a constant current of 100 pA to the circuits modeling the neurons PLML and PLMR. This reflects a continuously sensed gentle touch that should trigger forward locomotion. The utilized parameters are given in Tables. 1 and 2. Here, the ratio of the coupling strengths is taken from [1]. In the following, we first discuss the simulation results for the membrane potentials and fluorescence traces to verify that forward locomotion is indeed generated. Afterwards, we study energy consumption rates of the neuronal network occurring during this locomotion.

Results for the membrane potentials of all 279 neurons are depicted in the top panel of Fig. 12 and relative fluorescence traces can be seen in the center panel of Fig. 12. Motor neurons can be identified by their slowly

Table 2 Parameters for the coupling structure

Coupling network		
$G_{\mathrm{el}} = 90\mathrm{pS}$	$G_{\mathrm{Glu}} = 45\mathrm{pS}$	$E_{\mathrm{exc}} = 110\mathrm{mV}$
$U_{\mathrm{s1}} = -20\mathrm{mV}$	$G_{\mathrm{ACh}} = 45\mathrm{pS}$	$E_{\mathrm{inh}} = -120\mathrm{mV}$
$U_{\mathrm{s2}} = 0.1\mathrm{mV}$	$G_{\mathrm{GABA}} = 67.5\mathrm{pS}$	

oscillating activity pattern, see e.g. neurons labeled with 239–279. Interneurons exhibit a more or less constant membrane potential, see e.g. neurons labeled with 11–23. Activity of sensory neurons is given by fast oscillations, but is barely visible because there are no larger groups of active sensory neurons. Evaluating which neurons are active in particular, it turns out that almost all motor neurons, approximately 2/3 of all interneurons, and only 3 sensory neurons show activity. The latter are in particular the neurons PLML,PLMR, and ALM. Even though ALM is part of the backward locomotory circuit, this might be reasonable, as hints have been found that neurons of the mechanosensory system influence each other [42].

Taking a look at the muscle activity illustrated in the bottom panel of Fig. 12, we observe that after a transient phase of 10 s, activity within each muscle group is propagating approximately diagonally from low indices to high indices. Note that the transient phase is due to the neuron and muscle circuits being initialized near their resting states. The diagonally propagating activity is especially observable for the dorsal left (DL) and dorsal right (DR) muscles, and to a lesser extend also from the ventral left (VL) and ventral right (VR) muscles. In light of the fact that the muscles of these groups are arranged from head to tail with increasing index, these results suggest that locomotion is indeed generated.

5.3 Power consumption

Finally, we investigate the power consumption of the neuronal ion channels, neuronal synapses and gap junctions present in the neuronal network of *C. elegans*. Based on [43,44], the rate of energy consumption for the ion channels p_{ion} and gap junctions p_{gap}, equivalent to power, can be calculated via

$$p_{\mathrm{ion}} = \sum_{\mu=1}^{N} -i_{\mathrm{Ca},\mu}\left[u_{\mathrm{n},\mu} - E_{\mathrm{Ca},\mu}\right] \tag{15a}$$
$$- i_{\mathrm{K},\mu}\left[u_{\mathrm{n},\mu} - E_{\mathrm{K},\mu}\right] - i_{\mathrm{L},\mu}\left[u_{\mathrm{n},\mu} - E_{\mathrm{L},\mu}\right]$$
$$p_{\mathrm{gap}} = \mathbf{u}_{\mathrm{n}}\boldsymbol{\Lambda}_{\mathrm{el}}\mathbf{u}_{\mathrm{n}}^{T}, \ \mathbf{u}_{\mathrm{n}} = \left[u_{\mathrm{n},1} \ ... \ u_{\mathrm{n},N}\right]^{T}, \tag{15b}$$

where $\boldsymbol{\Lambda}_{\mathrm{el}}$ is a Laplacian matrix describing the connections via gap junctions. Following this approach, the energy consumption rate for the synapses is given by

$$p_{\mathrm{syn}} = \sum_{\mu=1}^{N} -j_{\mathrm{n},\mu}^{\mathrm{ACh}}\left[u_{\mathrm{n},\mu} - E_{\mathrm{exc}}\right]$$
$$- j_{\mathrm{n},\mu}^{\mathrm{Glu}}\left[u_{\mathrm{n},\mu} - E_{\mathrm{exc}}\right] - j_{\mathrm{n},\mu}^{\mathrm{GABA}}\left[u_{\mathrm{n},\mu} - E_{\mathrm{inh}}\right]. \tag{15c}$$

Calculating these energy consumption rates for the neuronal network of *C. elegans* during locomotion (cf. Figure 12), yields the results shown in Fig. 13. Comparing Fig. 13a, d, we find that the ion channels have by far the highest energy consumption rate. Gap junctions and synapses, on the other hand, account for only a
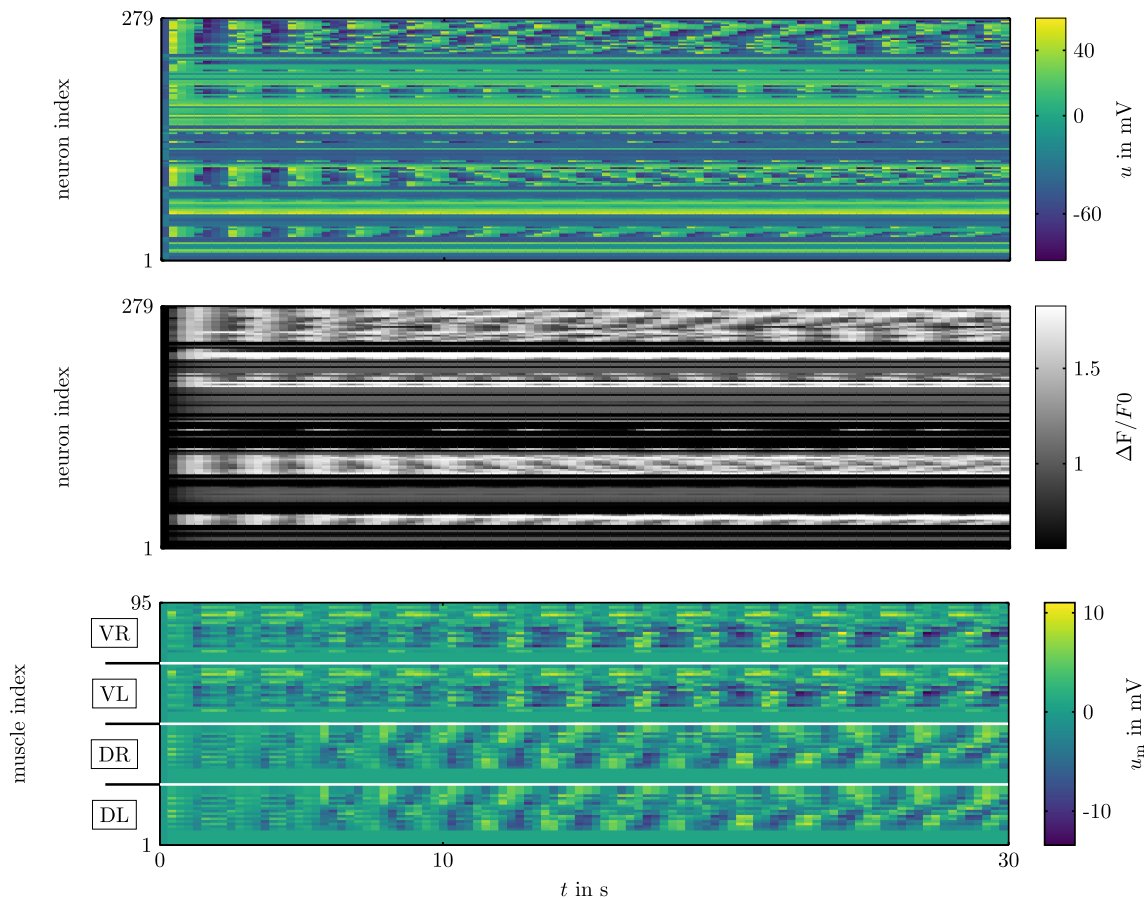
Fig. 12 Neuronal and muscular activity. Top: Membrane potentials of all 279 neurons. Center: Relative fluorescence traces of all 279 neurons. Bottom: Muscle activity of all 95 muscles. White lines are used to highlight the four different groups of muscles

small fraction of the consumed energy. From an energy-efficiency point of view, it seems advantageous to have small numbers of neurons but a large number of interconnections. This is supported by the fact that *C. elegans* possesses merely 300 neurons, but several thousand connections via gap junctions or synapses. Moreover, this suggests that neurons with a high degree of connectivity, such as interneurons, are especially important for an energy-efficient information processing.

Observing Fig. 13a, we see that the motor neurons show the highest energy consumption rate, followed by the inter and the sensory neurons. This is directly related to the fact that during locomotion, almost all motor neurons of the entire neuronal network are active, but only 2/3 of the interneurons and only three of the sensory neurons. Considering the average energy consumption rates of single, active neurons depicted in Fig. 13b shows that a motor neuron consumes the least amount of energy. A sensory neuron has the highest average energy consumption rate, although the rate fluctuates strongly due to the fast oscillating behavior of the sensory neurons. The average consumption rate of interneurons is only slightly lower than the one of a sensory neuron, but higher than that of a motor neuron by a factor of 1.6. This can be explained by

the isopotential behavior of the interneurons. This type of behavior implies that the neurons are constantly in a state that is not their resting state and hence constantly consume energy. Figure 13c presents the average energy consumption rates of individual sensory, inter, and motor neurons. The rates are ordered by how many neurons of each type are active during locomotion. The figure shows that the more energetically expensive a neuron type is, the less frequently it occurs. This supports the idea that the neuronal network is designed with respect to energy-efficiency.

From Fig. 13d, we can see that the energy consumption rate of the gap junctions is lower than that of the synapses by a factor of five. As there are 1028 gap junctions and 2005 synapses [1], the average energy consumption rate of a single gap junction and a single synapse is 0.3 pW and 0.82 pW, respectively. Hence, gap junctions consume less energy than synapses. This makes sense because gap junctions are represented by constant resistors in series to the neuron circuits and lead to synchronization effects. Synchronization of the neuronal membrane potentials in turn leads to extremely small voltage differences across the gap junction resistors, and as such, the dissipated powers are also very low.
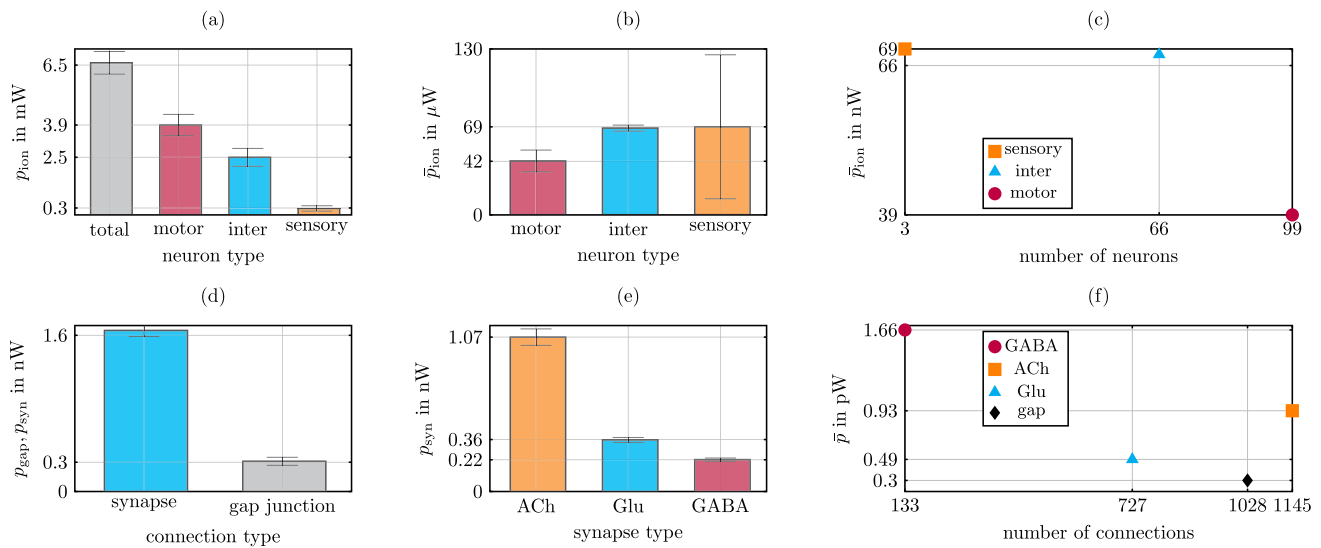
Fig. 13 Energy consumption rates. **a** Rates for the ion channels of all neurons, and **b** average rates for ion channels of a single, active neuron. **c** Comparison of average rates with respect to the number of active sensory, motor, and interneurons. **d** Rates for all gap junctions and synapses, and **e** rates for all synapses of a specific neurotransmitter type. **f** Average rates for a single synaptic or gap junctions connection vs the total number of connections present for the type of connection (i.e. ACh-synapse, GABA-synapse, Glu-synapse, gap junction)

Let us now take a look at the energy consumption rates of the different synapse types shown in Fig. 13e. It turns out that the sum of all ACh-sensitive synapses consumes the most energy, followed by Glu-sensitive synapses and GABA-sensitive synapses. Average consumption rates for single synapses with respect to how often their neurotransmitter type occurs are depicted in Fig. 13f. This shows that a single GABA-sensitive synapse consumes by far the most energy, followed by ACh-sensitive and Glu-sensitive synapses. Even in comparison to the single synapse types, gap junctions are still energetically cheaper. However, we can also see that energetically more expensive connections do not necessarily occur less frequently. In particular, even though ACh-sensitive synapses occur the most, they are energetically more expensive than, e.g., Glu-sensitive synapses. This indicates that a low energy-consumption is not the only design criterion for the neuronal network and that there probably is a balance, e.g., between ensuring functionality and keeping energy costs as low as possible.

6 Conclusion

In this work, we have designed an ideal electrical circuit modeling the somatic neuronal network and muscle system of *C. elegans*. For the neurons, we have used Morris–Lecar circuits in combination with RC circuits to calculate the membrane potential and a relative fluorescence of each neuron. The muscle circuits are based on a leaky integrator model, which translates into an RC circuit as well.

Simulation results of the complete circuit structure have shown that when applying an input current representing a gentle touch of the worm, a locomotion behavior can indeed be observed from the muscle activities. Results for the membrane potentials of the neurons have shown that despite simulating a forward locomotion, more than half of the entire neuronal network and almost all motor neurons are active instead of only the neurons typically associated with forward locomotion. It is very likely that this is due to the overall interconnection structure of the neurons, since experiments have been reported where, e.g., different neurons of the mechanosensory system influence each other.

In the second step, we have investigated the energy consumption rates occurring during the simulated locomotion. This has revealed that by far the most energy is consumed by the ion channels of the neurons and only a small fraction is consumed by gap junctions and synapses. Hence, a low number of neurons in contrast to a high number of interconnections is energetically favorable. This highlights the importance of strongly interconnected neurons such as interneurons. We have also considered the average energy consumption rates of the different neuron types with respect to the occurrences of the neuron types. This has shown that the more energy is consumed, the less likely a neuron type occurs in the neuronal network used for generating locomotion. Concerning the neuronal interconnections, our results have shown that gap junctions consume less energy than synapses and that from the synapses, GABA-sensitive ones are the energetically most expensive ones. Aver-

age energy consumption rates for the connection types with respect to their respective occurrences have mostly also shown the tendency that energetically expensive connections occur less frequently, with the exception of ACh-synapses. These occur the most frequently but are not the energetically cheapest connection type. As a design criterion for neuronal networks, there probably is some kind of balance between functionality and energy costs.

As a simulation technique, we have used a wave digital algorithm that is run-time efficient and potentially real-time capable and thus especially useful for simulating larger neuronal networks. Moreover, the algorithm retains the port-wise structure of the electrical circuit due to its direct correspondence with the circuit. This allows for plasticity studies of the *C. elegans* connectome that can be adjusted during the run-time of the simulation.

Author contributions

Sebastian Jenderny: Conceptualization, Methodology, Software, Validation, Writing—original draft. Karlheinz Ochs: Conceptualization, Validation, Writing—review and editing, Supervision. Philipp Hövel: Conceptualization, Software, Resources, Validation, Writing—review and editing.

Data Availability Statement Data will be made available on reasonable request.

Declarations

Conflict of interest The authors have no relevant financial or non-financial interests to disclose. PH currently serves as Associate Editor of EPJB and has not been involved in the review process of this manuscript.

Appendix A List of neurons

For the sake of completeness, we have listed the classification of *C. elegans* neurons considered in this work into sensory neurons, motor neurons, and interneurons in the following tables.

Table 3 Neurons with number 0–122 and their types

Index	Neuron	Type	Index	Neuron	Type	Index	Neuron	Type	Index	Neuron	Type	Index	Neuron	Type
0	ADAL	Inter	26	ALNR	Sensory	52	AUAR	Sensory	78	BAGL	Sensory	104	DD03	Motor
1	ADAR	Inter	27	AQR	Sensory	53	AVAL	Inter	79	BAGR	Sensory	105	DD04	Motor
2	ADEL	Sensory	28	AS01	Motor	54	AVAR	Inter	80	BDUL	Sensory	106	DD05	Motor
3	ADER	Sensory	29	AS02	Motor	55	AVBL	Inter	81	BDUR	Sensory	107	DD06	Motor
4	ADFL	Sensory	30	AS03	Motor	56	AVBR	Inter	82	CEPDL	Sensory	108	DVA	Inter
5	ADFR	Sensory	31	AS04	Motor	57	AVDL	Inter	83	CEPDR	Sensory	109	DVB	Inter
6	ADLL	Sensory	32	AS05	Motor	58	AVDR	Inter	84	CEPVL	Sensory	110	DVC	Inter
7	ADLR	Sensory	33	AS06	Motor	59	AVEL	Inter	85	CEPVR	Sensory	111	FLPL	Sensory
8	AFDL	Sensory	34	AS07	Motor	60	AVER	Inter	86	DA01	Motor	112	FLPR	Sensory
9	AFDR	Sensory	35	AS08	Motor	61	AVFL	Inter	87	DA02	Motor	113	HSNL	Motor
10	AIAL	Inter	36	AS09	Motor	62	AVFR	Inter	88	DA03	Motor	114	HSNR	Motor
11	AIAR	Inter	37	AS10	Motor	63	AVG	Inter	89	DA04	Motor	115	IL1DL	Sensory
12	AIBL	Inter	38	AS11	Motor	64	AVHL	Sensory	90	DA05	Motor	116	IL1DR	Sensory
13	AIBR	Inter	39	ASEL	Sensory	65	AVHR	Sensory	91	DA06	Motor	117	IL1L	Sensory
14	AIML	Inter	40	ASER	Sensory	66	AVJL	Sensory	92	DA07	Motor	118	IL1R	Sensory
15	AIMR	Inter	41	ASGL	Sensory	67	AVJR	Sensory	93	DA08	Motor	119	IL1VL	Sensory
16	AINL	Inter	42	ASGR	Sensory	68	AVKL	Inter	94	DA09	Motor	120	IL1VR	Sensory
17	AINR	Inter	43	ASHL	Sensory	69	AVKR	Inter	95	DB01	Motor	121	IL2DL	Sensory
18	AIYL	Inter	44	ASHR	Sensory	70	AVL	Inter	96	DB02	Motor	122	IL2DR	Sensory
19	AIYR	Inter	45	ASIL	Sensory	71	AVM	Sensory	97	DB03	Motor	123	IL2L	Sensory
20	AIZL	Inter	46	ASIR	Sensory	72	AWAL	Sensory	98	DB04	Motor	124	IL2R	Sensory
21	AIZR	Inter	47	ASJL	Sensory	73	AWAR	Sensory	99	DB05	Motor	125	IL2VL	Sensory
22	ALA	Inter	48	ASJR	Sensory	74	AWBL	Sensory	100	DB06	Motor	126	IL2VR	Sensory
23	ALML	Sensory	49	ASKL	Sensory	75	AWBR	Sensory	101	DB07	Motor	127	LUAL	Inter
24	ALMR	Sensory	50	ASKR	Sensory	76	AWCL	Sensory	102	DD01	Motor	128	LUAR	Inter
25	ALNL	Sensory	51	AUAL	Sensory	77	AWCR	Sensory	103	DD02	Motor	129	OLLL	Sensory

Table 4 Neurons with number 130–278 and their types

Index	Neuron	Type	Index	Neuron	Type	Index	Neuron	Type	Index	Neuron	Type	Index	Neuron	Type
130	OLLR	Sensory	160	PVQR	Inter	190	RMDVR	Motor	220	SMBVL	Motor	250	VB01	Motor
131	OLQDL	Sensory	161	PVR	Inter	191	RMED	Motor	221	SMBVR	Motor	251	VB02	Motor
132	OLQDR	Sensory	162	PVT	Inter	192	RMEL	Motor	222	SMDDL	Motor	252	VB03	Motor
133	OLQVL	Sensory	163	PVWL	Inter	193	RMER	Motor	223	SMDDR	Motor	253	VB04	Motor
134	OLQVR	Sensory	164	PVWR	Inter	194	RMEV	Motor	224	SMDVL	Motor	254	VB05	Motor
135	PDA	Motor	165	RIAL	Inter	195	RMFL	Motor	225	SMDVR	Motor	255	VB06	Motor
136	PDB	Motor	166	RIAR	Inter	196	RMFR	Motor	226	URADL	Motor	256	VB07	Motor
137	PDEL	Sensory	167	RIBL	Inter	197	RMGL	Inter	227	URADR	Motor	257	VB08	Motor
138	PDER	Sensory	168	RIBR	Inter	198	RMGR	Inter	228	URAVL	Motor	258	VB09	Motor
139	PHAL	Sensory	169	RICL	Inter	199	RMHL	Motor	229	URAVR	Motor	259	VB10	Motor
140	PHAR	Sensory	170	RICR	Inter	200	RMHR	Motor	230	URBL	Inter	260	VB11	Motor
141	PHBL	Sensory	171	RID	Inter	201	SAADL	Inter	231	URBR	Inter	261	VC01	Motor
142	PHBR	Sensory	172	RIFL	Inter	202	SAADR	Inter	232	URXL	Inter	262	VC02	Motor
143	PHCL	Sensory	173	RIFR	Inter	203	SAAVL	Inter	233	URXR	Inter	263	VC03	Motor
144	PHCR	Sensory	174	RIGL	Inter	204	SAAVR	Inter	234	URYDL	Sensory	264	VC04	Motor
145	PLML	Sensory	175	RIGR	Inter	205	SABD	Inter	235	URYDR	Sensory	265	VC05	Motor
146	PLMR	Sensory	176	RIH	Inter	206	SABVL	Inter	236	URYVL	Sensory	266	VD01	Motor
147	PLNL	Inter	177	RIML	Inter	207	SABVR	Inter	237	URYVR	Sensory	267	VD02	Motor
148	PLNR	Inter	178	RIMR	Inter	208	SDQL	Inter	238	VA01	Motor	268	VD03	Motor
149	PQR	Sensory	179	RIPL	Inter	209	SDQR	Inter	239	VA02	Motor	269	VD04	Motor
150	PVCL	Inter	180	RIPR	Inter	210	SIADL	Inter	240	VA03	Motor	270	VD05	Motor
151	PVCR	Inter	181	RIR	Inter	211	SIADR	Inter	241	VA04	Motor	271	VD06	Motor
152	PVDL	Sensory	182	RIS	Inter	212	SIAVL	Inter	242	VA05	Motor	272	VD07	Motor
153	PVDR	Sensory	183	RIVL	Inter	213	SIAVR	Inter	243	VA06	Motor	273	VD08	Motor
154	PVM	Sensory	184	RIVR	Inter	214	SIBDL	Inter	244	VA07	Motor	274	VD09	Motor
155	PVNL	Inter	185	RMDDL	Motor	215	SIBDR	Inter	245	VA08	Motor	275	VD10	Motor
156	PVNR	Inter	186	RMDDR	Motor	216	SIBVL	Inter	246	VA09	Motor	276	VD11	Motor
157	PVPL	Inter	187	RMDL	Motor	217	SIBVR	Inter	247	VA10	Motor	277	VD12	Motor
158	PVPR	Inter	188	RMDR	Motor	218	SMBDL	Motor	248	VA11	Motor	278	VD13	Motor
159	PVQL	Inter	189	RMDVL	Motor	219	SMBDR	Motor	249	VA12	Motor			

References

1. T. Maertens, E. Schöll, J. Ruiz, P. Hövel, Multilayer network analysis of *C. elegans*: looking into the locomotory circuitry. Neurocomputing **427**, 238–261 (2021). https://doi.org/10.1016/j.neucom.2020.11.015

2. Z.F. Altun, D.H. Hall, Muscle system, somatic muscle. WormAtlas (2009). https://doi.org/10.3908/wormatlas.1.7

3. B.G. Sakelaris, Z. Li, J. Sun, S. Banerjee, V. Booth, E. Gourgou, Modelling learning in caenorhabditis elegans chemosensory and locomotive circuitry for t-maze navigation. Eur. J. Neurosci. **55**(2), 354–376 (2022). https://doi.org/10.1111/ejn.15560

4. H. Chen, Q. Hong, Z. Wang, C. Wang, Z. X. Zeng, J. Zhang, Memristive circuit implementation of caenorhabditis elegans mechanism for neuromorphic computing. IEEE Trans. Neural Netw. Learn. Syst. 1–12 (2023). https://doi.org/10.1109/TNNLS.2023.3250655

5. L. Yu, Y. Yu, Energy-efficient neural information processing in individual neurons and neuronal networks. J. Neurosci. Res. **95**(11), 2253–2266 (2017). https://doi.org/10.1002/jnr.24131

6. G. Wang, R. Wang, W. Kong, J. Zhang, The relationship between sparseness and energy consumption of neural networks. Neural Plast. **2020**, 1–13 (2020). https://doi.org/10.1155/2020/8848901

7. R.C. Vergara, S. Jaramillo-Riveri, A. Luarte, C. Moënne-Loccoz, R. Fuentes, A. Couve, P.E. Maldonado, The energy homeostasis principle: Neuronal energy regulation drives local network dynamics generating behavior. Front. Comput. Neurosci. **13** (2019. https://doi.org/10.3389/fncom.2019.00049

8. S. Li, C. Yan, Y. Liu, Energy efficiency and coding of neural network. Front. Neurosci. **16** (2023). https://doi.org/10.3389/fnins.2022.1089373

9. P. Machado, J. Wade, T. M. McGinnity, Si elegans: FPGA hardware emulation of *C. elegans* nematode nervous system. In: 2014 Sixth World Congress on Nature and Biologically Inspired Computing (NaBIC 2014), 65–71 (2014). https://doi.org/10.1109/NaBIC.2014.6921855

10. P. Machado, J. Wade, T.M. McGinnity, Si elegans: modeling the *C. elegans* nematode nervous system using high performance FPGAS, pp. 31–45. Springer, Cham (2016). https://doi.org/10.1007/978-3-319-26242-0_3

11. A. Fettweis, Wave digital filters: theory and practice. Proc. IEEE **74**(2), 270–327 (1986). https://doi.org/10.1109/PROC.1986.13458

12. K. Ochs, D. Michaelis, S. Jenderny, An optimized Morris–Lecar neuron model using wave digital principles. In: 2018 IEEE 61st International Midwest Symposium on Circuits and Systems (MWSCAS), 61–64 (2018). https://doi.org/10.1109/MWSCAS.2018.8623905

13. S. Jenderny, K. Ochs, Wave digital model of calcium-imaging-based neuronal activity of mice. Int. J. Numer. Modell. Electron. Netw. Dev. Fields **36**(2), 3053 (2023). https://doi.org/10.1002/jnm.3053

14. S. Jenderny, K. Ochs, Wave digital emulation of a bio-inspired circuit for axon growth. In: 2022 IEEE Biomedical Circuits and Systems Conference (BioCAS), pp. 260–264 (2022). https://doi.org/10.1109/BioCAS54905.2022.9948613

15. J. Mellem, P. Brockie, D. Madsen, A. Maricq, Action potentials contribute to neuronal signaling in *C. elegans.* Nat. Neurosci. 11, 865–7 (2008. https://doi.org/10.1038/nn.2131

16. Q. Liu, P.B. Kidd, M. Dobosiewicz, C.I. Bargmann, C. elegans AWA olfactory neurons fire calcium-mediated all-or-none action potentials. Cell **175**(1), 57–7017 (2018) https://doi.org/10.1016/j.cell.2018.08.018

17. S. Faumont, T. Lindsay, S. Lockery, Neuronal microcircuits for decision making in *C. elegans.* Curr. Opin. Neurobiol. **22**(4), 580–591 (2012). https://doi.org/10.1016/j.conb.2012.05.005

18. J. Jiang, Y. Su, R. Zhang, H. Li, L. Tao, Q. Liu, *C. elegans* enteric motor neurons fire synchronized action potentials underlying the defecation motor program. Nat. Commun. **13** (2022) https://doi.org/10.1038/s41467-022-30452-y

19. Z.F. Altun, L.A. Herndon, C.A. Wolkow, C. Crocker, R. Lints, D.H. Hall, Worm Atlas. http://www.wormatlas.org. Accessed March 18, 2024 (2023)

20. S. Lockery, M. Goodman, The quest for action potentials in *C. elegans* neurons hits a plateau. Nat. Neurosci. **12**, 377–8 (2009). https://doi.org/10.1038/nn0409-377

21. J. Gjorgjieva, D. Biron, G. Haspel, Neurobiology of Caenorhabditis elegans locomotion: where do we stand? BioScience **64**(6), 476–486 (2014). https://doi.org/10.1093/biosci/biu058

22. S. Gao, S.A. Guan, A.D. Fouad, J. Meng, T. Kawano, Y.-C. Huang, Y. Li, S. Alcaire, W. Hung, Y. Lu, Y.B. Qi, Y. Jin, M. Alkema, C. Fang-Yen, M. Zhen, Excitatory motor neurons are local oscillators for backward locomotion. eLife **7**, 29915 (2018) https://doi.org/10.7554/eLife.29915

23. C. Morris, H. Lecar, Voltage oscillations in the barnacle giant muscle fiber. Biophys. J. **35**(1), 193–213 (1981). https://doi.org/10.1016/S0006-3495(81)84782-0

24. V. Rajamani, M. Sah, Z. Mannan, H. Kim, L. Chua, Third-order memristive morris-lecar model of barnacle muscle fiber. Int. J. Bifurcat. Chaos **27**(4) (2017). https://doi.org/10.1142/S0218127417300154

25. M. Nicoletti, A. Loppini, L. Chiodo, V. Folli, G. Ruocco, S. Filippi, Biophysical modeling of C. elegans neurons: single ion currents and whole-cell dynamics of awcon and rmd. Plos One **14**(7), 1–33 (2019). https://doi.org/10.1371/journal.pone.0218738

26. J.P. Nguyen, F.B. Shipley, A.N. Linder, G.S. Plummer, M. Liu, S.U. Setru, J.W. Shaevitz, A.M. Leifer, Whole-brain calcium imaging with cellular resolution in freely behaving Caenorhabditis elegans. Proc. Natl. Acad. Sci. **113**(8), 1074–1081 (2016). https://doi.org/10.1073/pnas.1507110112

27. H. Li, F. Feng, M. Zhai, J. Zhang, J. Jiang, Y. Su, L. Chen, S. Gao, L. Tao, H. Mao, Fast whole-body motor neuron calcium imaging of freely moving caenorhabditis elegans without coverslip pressed. Cytometry Part

28. K. M. Hallinen, R. Dempsey, M. Scholz, X. Yu, A. Linder, F. Randi, A. K. Sharma, J. W. Shaevitz, A. M. Leifer, Decoding locomotion from population neural activity in moving *C. elegans.* eLife **10**, 66135 (2021). https://doi.org/10.7554/eLife.66135

A **99**(11), 1143–1157 (2021). https://doi.org/10.1002/cyto.a.24483

29. M. Maravall, Z.F. Mainen, B.L. Sabatini, K. Svoboda, Estimating intracellular calcium concentrations and buffering without wavelength ratioing. Biophys. J. **78**(5), 2655–2667 (2000). https://doi.org/10.1016/S0006-3495(00)76809-3

30. M. Bootman, K. Rietdorf, T. Collins, S. Walker, M. Sanderson, Converting fluorescence data into Ca^{2+} concentration. Cold Spring Harbor protocols **2013** (2013). https://doi.org/10.1101/pdb.prot072827

31. T.-W. Chen, T. Wardill, Y. Sun, S. Pulver, S. Renninger, A. Baohan, E. Schreiter, R. Kerr, M. Orger, V. Jayaraman, L. Looger, K. Svoboda, D. Kim, Ultrasensitive fluorescent proteins for imaging neuronal activity. Nature **499**, 295–300 (2013). https://doi.org/10.1038/nature12354

32. J. Boyle, S. Berri, N.Cohen, Gait modulation in c. elegans: an integrated neuromechanical model. Front. Comput. Neurosci. **6** (2012). https://doi.org/10.3389/fncom.2012.00010

33. E.J. Izquierdo, R.D. Beer, From head to tail: a neuromechanical model of forward locomotion in Caenorhabditis elegans. Philos. Trans. R. Soc. B: Biol. Sci. **373**(1758), 20170374 (2018). https://doi.org/10.1098/rstb.2017.0374

34. E. Olivares, E. J. Izquierdo, R. D. Beer, A neuromechanical model of multiple network rhythmic pattern generators for forward locomotion in *C. elegans.* Front. Comput. Neurosci. **15** (2021. https://doi.org/10.3389/fncom.2021.572339

35. J. Winters, An improved muscle-reflex actuator for use in large-scale neuromusculoskeletal models. Ann. Biomed. Eng. **23**, 359–74 (1995). https://doi.org/10.1007/BF02584437

36. P. Feketa, T. Birkoben, M. Noll, A. Schaum, T. Meurer, H.Kohlstedt, artificial homeostatic temperature regulation via bio-inspired feedback mechanisms. Sci. Rep. **13** (2023). https://doi.org/10.1038/s41598-023-31963-4

37. A. Meerkötter, Digital realization of connection networks by voltage-wave two-port adaptors. AEÜ Int. J. Electron. Commun. **50**(6), 362–367 (1996). https://doi.org/10.1109/PROC.1986.13458

38. K. Ochs, B. A. Beattie, Towards wave digital modeling of neural pathways using two-port coupling networks. In: 2022 IEEE International Symposium on Circuits and Systems (ISCAS), pp. 809–812 (2022). https://doi.org/10.1109/ISCAS48785.2022.9937250

39. T. Schwerdtfeger, A. Kummert, Nonlinear circuit simulation by means of alfred Fettweis' wave digital principles. IEEE Circ. Syst. Mag. **19**(1), 55–65 (2019). https://doi.org/10.1109/MCAS.2018.2872666

40. A. Proverbio, A. Bernardini, A. Sarti, Toward the wave digital real-time emulation of audio circuits with multiple nonlinearities. In: 2020 28th European Signal Processing Conference (EUSIPCO), pp. 151–155 (2021). https://doi.org/10.23919/Eusipco47968.2020.9287449. (2020 28th European Signal Processing Conference (EUSIPCO))

41. A. Bernardini, E. Bozzo, F. Fontana, A. Sarti, A wave digital newton-raphson method for virtual analog modeling of audio circuits with multiple one-port nonlinearities. IEEE/ACM Transactions on Audio, Speech, and Language Processing, pp. 1–1 (2021). https://doi.org/10.1109/TASLP.2021.3084337

42. W. Schafer, Mechanosensory molecules and circuits in *C. elegans*. Pflugers Archiv : Eur. J. Physiol. **467** (2014). https://doi.org/10.1007/s00424-014-1574-3

43. A. Moujahid, A. d'Anjou, F.J. Torrealdea, F. Torrealdea, Energy and information in hodgkin–huxley neurons. Phys. Rev. E **83**, 031912 (2011). https://doi.org/10.1103/PhysRevE.83.031912

44. Y. Wang, R. Wang, X. Xu, Neural energy supply-consumption properties based on hodgkin–huxley model. Neural Plast. **2017**, 1–11 (2017). https://doi.org/10.1155/2017/6207141